Combined first-principles and model Hamiltonian study of the perovskite series RMnO$_3$ (R = La, Pr, Nd, Sm, Eu, and Gd)

Roman Kováčik,[1,*] Sowmya Sathyanarayana Murthy,[2] Carmen E. Quiroga,[3] Claude Ederer,[4] and Cesare Franchini[2]

[1]*Peter Grünberg Institut and Institute for Advanced Simulation, Forschungszentrum Jülich and JARA, 52425 Jülich, Germany*
[2]*Faculty of Physics, University of Vienna, Sensengasse 8/8, A-1090 Wien, Austria*
[3]*Department of Earth and Environmental Sciences, Ludwig-Maximillians-Universität München, Theresienstrasse 41, 80333 München, Germany*
[4]*Materials Theory, ETH Zürich, Wolfgang-Pauli-Strasse 27, 8093 Zürich, Switzerland*

We merge advanced *ab initio* schemes (standard density functional theory, hybrid functionals, and the GW approximation) with model Hamiltonian approaches (tight-binding and Heisenberg Hamiltonian) to study the evolution of the electronic, magnetic, and dielectric properties of the manganite family RMnO$_3$ (R = La, Pr, Nd, Sm, Eu, and Gd). The link between first principles and tight binding is established by downfolding the physically relevant subset of $3d$ bands with e_g character by means of maximally localized Wannier functions (MLWFs) using the VASP2WANNIER90 interface. The MLWFs are then used to construct a general tight-binding Hamiltonian written as a sum of the kinetic term, the Hund's rule coupling, the JT coupling, and the electron-electron interaction. The dispersion of the tight-binding (TB) e_g bands at all levels are found to match closely the MLWFs. We provide a complete set of TB parameters which can serve as guidance for the interpretation of future studies based on many-body Hamiltonian approaches. In particular, we find that the Hund's rule coupling strength, the Jahn-Teller coupling strength, and the Hubbard interaction parameter U remain nearly constant for all the members of the RMnO$_3$ series, whereas the nearest-neighbor hopping amplitudes show a monotonic attenuation as expected from the trend of the tolerance factor. Magnetic exchange interactions, computed by mapping a large set of hybrid functional total energies onto an Heisenberg Hamiltonian, clarify the origin of the A-type magnetic ordering observed in the early rare-earth manganite series as arising from a net negative out-of-plane interaction energy. The obtained exchange parameters are used to estimate the Néel temperature by means of Monte Carlo simulations. The resulting data capture well the monotonic decrease of the ordering temperature down the series from R = La to Gd, in agreement with experiments. This trend correlates well with the modulation of structural properties, in particular with the progressive reduction of the Mn-O-Mn bond angle which is associated with the quenching of the volume and the decrease of the tolerance factor due to the shrinkage of the ionic radii of R going from La to Gd.

I. INTRODUCTION

Perovskite transition metal oxides (TMOs), which fall under the category of strongly correlated systems, exhibit a wide array of complex orbitally and spin ordered states, arising from the interplay of the structural, electronic, and magnetic degrees of freedom. In particular, rare-earth manganites with the general formula $R_{1-x}A_x$MnO$_3$, where R is a trivalent rare-earth cation and A is a divalent alkaline-earth cation, exhibit stunning characteristics such as the colossal magnetoresistance (CMR) effect [1–5], observed in compounds like Pr$_{1-x}$Ca$_x$MnO$_3$, Pr$_{1-x}$Ba$_x$MnO$_3$, Nd$_{0.5}$Sr$_{0.5}$MnO$_3$, and in the well-known hole-doped LaMnO$_3$ [6,7]. Another interesting property, tuned by the Mn^{3+} magnetic structure variation in RMnO$_3$ [8], is the emergence of magnetoelectric/multiferroic properties for the smaller rare-earth cations (R = Gd, Tb, Dy) [9,10]. Despite the large number of studies on CMR and parent CMR compounds, experimental [11–20] and theoretical studies [21–29] on early RMnO$_3$ are found in less numbers.

The phase diagram of RMnO$_3$ (Fig. 1) reported by Kimura *et al.* [8] shows the trends of the orbital (T_{OO}) and the spin (T_N) ordering temperatures as a function of the in-plane Mn-O-Mn angle ϕ_{ab}. It also illustrates that when the La^{3+} cation is replaced by smaller cations, a successive increase in the orthorhombic distortion, manifested by the decrease of ϕ_{ab}, is observed. The orbital ordering temperature T_{OO} monotonically increases with the decreasing atomic radius r_R of cation R, whereas the spin-ordering temperature T_N decreases steadily from 140 K for LaMnO$_3$ to 40 K for GdMnO$_3$ with decreasing r_R. The Mn-O-Mn bond angle is reduced by the smaller R^{3+} ion at the A site, which in turn increases the tilting of the oxygen octahedra, thereby weakening the A-type antiferromagnetic (A-AFM) order, characterized by an in-plane parallel alignment of spins antiparallelly coupled to the spins in adjacent planes.

Understanding the microscopic details of the manganite systems could help to gain insights into the fundamental physics behind these interesting phenomena. Theoretically, TMOs have been historically studied using two different approaches: *ab initio* and model Hamiltonians typically based on a tight-binding parametrization. With regard to first-principles calculations on RMnO$_3$, particularly detailed and interesting theoretical findings have been reported by Yamauchi *et al.* [21], where the authors discuss the validity of the commonly used generalized gradient approximation (GGA) to the exchange-correlation (XC) functional within the density functional theory (DFT) for RMnO$_3$ compounds.
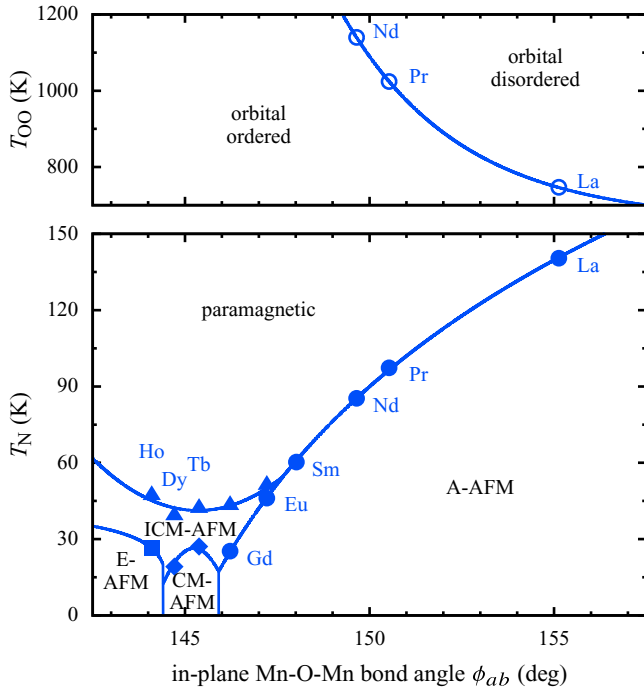
*r.kovacik@fz-juelich.de

FIG. 1. Phase diagram of the orbital (top) and spin (bottom) order in the early series of RMnO$_3$ as a function of the in-plane Mn-O-Mn bond angle ϕ_{ab}. Adapted from Ref. [8].

By adopting the fully optimized structure, it was shown that the Jahn-Teller (JT) distortion, typical of manganite systems and manifested by an alternating Mn-O bond length disproportionation, is underestimated using GGA. In agreement with the earlier study of Yin *et al.* [30], the situation in LaMnO$_3$ improves by incorporating an on-site Hubbard U parameter to the GGA or to the local density approximation (LDA), while for the other compounds in the series the agreement with the experimental structural data worsens. Similarly, the orthorhombic distortion in the whole series is better captured using the GGA approach. Finally, for values of $U \geqslant 4$ eV, the ferromagnetic (FM) ordering becomes the most favorable contrary to the experimental observation of A-AFM ordering. However, the deficiency of GGA in predicting the magnetic properties was also pointed out. While experiments have shown that at $T = 0$ K, the A-AFM state is the spin ground state even in GdMnO$_3$, GGA shows a total-energy trend where the E-type AFM (E-AFM) and the A-AFM phases are degenerate in SmMnO$_3$ and the E-AFM phase is found to be the most stable ordering for GdMnO$_3$.

In this study, we aim to investigate the evolution of the electronic and magnetic properties in the early series of RMnO$_3$ ($R = $ La, Pr, Nd, Sm, Eu, Gd). By combining first-principles calculations and the tight binding (TB) approach via maximally localized Wannier functions (MLWFs), we calculate the TB parameters by applying the methodology that was described in Ref. [28] for LaMnO$_3$. Two alternative model parametrizations are considered, which account for the effects of the electron-electron (el-el) interaction either implicitly in the otherwise non-interacting TB parameters or explicitly via a mean-field el-el interaction term in the TB Hamiltonian. Using this methodology, we explore the changes in the band
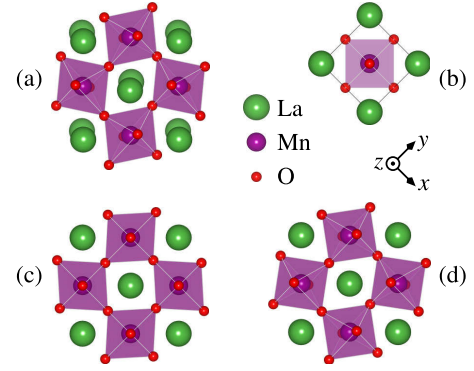

FIG. 2. (a) The experimental RMnO$_3$ crystal structure (example of $R = $ La) with distortion modes imposed on (b) the simple cubic perovskite structure: (c) the pure JT Q^x mode distortion and (d) the pure GFO-type distortion. Structural models were generated with VESTA [37]. Adapted from Fig. 1 in Ref. [38].

structure of RMnO$_3$ and construct, compare, and interpret the obtained TB parameters. Different levels of approximation to the XC kernel are adopted: standard DFT within GGA, hybrid functionals, and GW. Thereby a ready-to-use set of TB parameters is provided for future studies.

We will start with a brief overview of the basic ground-state properties of the RMnO$_3$ series (Sec. II) followed by two methodological sections focused on the description of the tight-binding parametrization (Sec. III) and the *ab initio* calculations (Sec. IV). The results for the electronic structure, magnetic properties, and tight-binding parameters are presented and discussed in Sec. V. The paper ends with a brief summary and conclusions.

II. RMnO$_3$ SERIES: FUNDAMENTALS

The ground-state electronic structure of RMnO$_3$ ($R = $ La, Pr, Nd, Sm, Eu, and Gd) is characterized by the crystal-field induced breaking of the degeneracy of the Mn^{3+} $3d^4$ manifold in the high-spin configuration $(t_{2g})^3 (e_g)^1$, with the t_{2g} orbitals lying lower in energy than the twofold degenerate e_g ones. Due to the strong Hund's rule coupling, the spins in the fully occupied majority t_{2g} orbitals ($S = 3/2$) are aligned parallel to the spin in the singly occupied majority e_g state ($S = 1/2$) at the same site. The orbital degeneracy in the e_g channel is further lifted via cooperative Jahn-Teller distortions [11,31–33], manifested by long and short Mn-O octahedral bonds alternating within the conventional orthorhombic basal plane, which are accompanied by GdFeO$_3$-type (GFO) checkerboard tilting and rotations of oxygen octahedra [34–36] (see Fig. 2). As a result, the ideal cubic perovskite structure is strongly distorted into an orthorhombic structure with *Pbnm* symmetry [34,35] and it has been experimentally confirmed that the orbital ordering is of C type, where the occupied e_g orbitals follow the checkerboard JT distortion pattern in the xy plane and the planes are stacked along the z axis [39]. The occupied e_g orbital can be represented by a linear combination of the d_{z^2} and $d_{x^2-y^2}$ character orbitals as $|\theta\rangle = \cos\frac{\theta}{2}|3z^2 - r^2\rangle + \sin\frac{\theta}{2}|x^2 - y^2\rangle$, where θ is the orbital mixing angle [30,40–42].
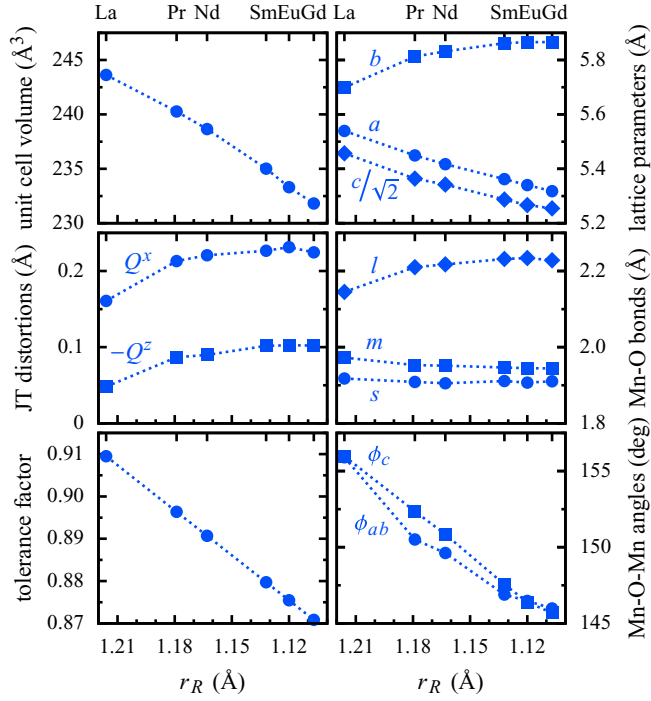
FIG. 3. Dependence of various structural parameters on the R cation radius r_R, taken or calculated from the experimental crystal structures at room temperature. Data for $R = $ La are taken from Ref. [35]; $R = $ Pr, Nd from Ref. [43]; $R = $ Sm, Eu, Gd from Ref. [44]. The tolerance factor is calculated using the Shannon radii of ninefold coordinated R^{3+} ions: $r_R = 1.216, 1.179, 1.163, 1.132, 1.120,$ and 1.107 Å for La, Pr, Nd, Sm, Eu, and Gd, respectively [45].

The most important structural characteristics as a function of the rare-earth cation radius r_R are collected in Fig. 3. As r_R decreases from La to Gd, the major effect is the unit-cell volume V reduction associated with the progressive decrease of the lattice parameters a and c (the so-called "lanthanide contraction"). In Ref. [43], it was pointed out that the characteristic relation $c/\sqrt{2} < a < b$ has its origin in the strong cooperative JT effect, inducing orbital ordering and distorting the MnO$_6$ octahedra. The local JT distortion modes are defined as $Q^x = (l - s)/\sqrt{2}$ and $Q^z = (2m - l - s)/\sqrt{6}$, where l, s, and m stand for long, short, and medium Mn-O bond lengths, respectively. From the trend shown in Fig. 3, a sizable increase of both $|Q^z|$ and Q^x can be seen in all members of the series as compared to LaMnO$_3$, stemming from the increase in l while m and s remain almost unchanged.

Another important quantity in the physics of ABO$_3$ compounds is the tolerance factor t [46], which gives an indication on the degree of structural distortions and the stability of the perovskite crystal structure. It can be defined as $t = (r_A + r_O)/[\sqrt{2}(r_B + r_O)]$, where r_A, r_B, and r_O are the ionic radii of A, B, and O, respectively. For the simple cubic perovskite structure, $t = 1$. Depending on the magnitude of t, different crystal structures are formed. In RMnO$_3$, the $A = R$ cations are too small to completely fill the space in the cubic structure. In this situation, the MnO$_6$ octahedra undergo collective rotations to maximize the space filling, thereby reducing the Mn-O-Mn bond angles from the ideal

$180°$. Clearly, the trend of the tolerance factor t is in accordance with the trend of the Mn-O-Mn bond angles. According to Zhou and Goodenough [47,48], the transition temperature T_N depends linearly on $\langle \cos^2 \phi \rangle$, where the average is taken over the three distinguishable Mn-O-Mn bond angles, i.e., the two ϕ_{ab} bond angles in the ab plane and the ϕ_c bond angle in the c direction.

III. METHODOLOGY: TIGHT-BINDING PARAMETERIZATION

Within the TB formalism, the effective electronic Hamiltonian of the e_g character manifold in manganites is generally written as a sum of the following contributions: the kinetic-energy term $\hat{H}_{\text{kin}}$ and several local interaction terms such as the Hund's rule coupling to the t_{2g} core spin $\hat{H}_{\text{Hund}}$, the JT coupling to the oxygen octahedra distortion $\hat{H}_{\text{JT}}$ and the electron-electron interaction $\hat{H}_{\text{el-el}}$ [28,38,49,50]:

$$\hat{H}_{\text{kin}} = -\sum_{\substack{\boldsymbol{R}, \Delta\boldsymbol{R}, \sigma \\ a, b}} \hat{c}_{a(\boldsymbol{R}+\Delta\boldsymbol{R})}^{\sigma\dagger} t_{a(\boldsymbol{R}+\Delta\boldsymbol{R})b(\boldsymbol{R})}^{\sigma} \hat{c}_{b(\boldsymbol{R})}^{\sigma}, \quad (1)$$

$$\hat{H}_{\text{Hund}} = -J_{\text{H}} \sum_{\substack{\boldsymbol{R}, \sigma, \sigma' \\ a}} \boldsymbol{S}_{\boldsymbol{R}} \hat{c}_{a(\boldsymbol{R})}^{\sigma\dagger} \boldsymbol{\tau}_{\sigma\sigma'} \hat{c}_{a(\boldsymbol{R})}^{\sigma'}, \quad (2)$$

$$\hat{H}_{\text{JT}} = -\lambda \sum_{\substack{\boldsymbol{R}, \sigma, i \\ a, b}} \hat{c}_{a(\boldsymbol{R})}^{\sigma\dagger} Q_{\boldsymbol{R}}^{i} \tau_{ab}^{i} \hat{c}_{b(\boldsymbol{R})}^{\sigma}, \quad (3)$$

$$\hat{H}_{\text{el-el}} = \frac{1}{2} \sum_{\substack{\boldsymbol{R}, \sigma, \sigma' \\ a, b, c, d}} U_{abcd} \hat{c}_{a(\boldsymbol{R})}^{\sigma\dagger} \hat{c}_{b(\boldsymbol{R})}^{\sigma'\dagger} \hat{c}_{d(\boldsymbol{R})}^{\sigma'} \hat{c}_{c(\boldsymbol{R})}^{\sigma}. \quad (4)$$

The annihilation $\hat{c}_{a(\boldsymbol{R})}^{\sigma}$ and the creation $\hat{c}_{a(\boldsymbol{R})}^{\sigma\dagger}$ operators are associated with orbital $|a\rangle$ at a particular Mn site $\boldsymbol{R}$ (not to be confused with cation R) and spin σ. In the kinetic-energy term, $t_{a(\boldsymbol{R}+\Delta\boldsymbol{R})b(\boldsymbol{R})}^{\sigma}$ is the hopping parameter between orbital $|b\rangle$ at site $\boldsymbol{R}$ and orbital $|a\rangle$ at site $\boldsymbol{R} + \Delta\boldsymbol{R}$. Further on, J_{H} is the Hund's rule strength of coupling to the normalized t_{2g} core spin $\boldsymbol{S}_{\boldsymbol{R}}$, λ is the JT coupling constant, $Q_{\boldsymbol{R}}^{i}$ is the amplitude of the particular JT mode ($i = \{x, z\}$) and τ_{ab}^{i} are the standard Pauli matrices. In this study, the electron-electron interaction term is treated within a mean-field approximation following the approach of Dudarev *et al.* [51], involving a single parameter $U_{\text{W}} = U_{aaaa} = U_{abab}$, with all other interaction matrix elements set to zero.

To obtain the model parameters we have extended the work presented in Ref. [28] to the RMnO$_3$ early series, wherein the model parameters are obtained from the Hamiltonian matrix elements in the MLWF basis. We will use a simplified notation for the MLWF matrix elements with the two basis functions of $|3z^2 - r^2\rangle$ and $|x^2 - y^2\rangle$ character centered at the same site. Thereby, the MLWF matrix element $h_{mn}^{\Delta\boldsymbol{T}}$, where $\Delta\boldsymbol{T}$ is the lattice translation and m and n are general orbital-site indices, can be written as $h_{mn}^{\Delta\boldsymbol{T}} \rightarrow h_{a\boldsymbol{R},b\boldsymbol{R}'}^{\Delta\boldsymbol{T}} \rightarrow h_{ab}^{\Delta\boldsymbol{R}}$, where $\Delta\boldsymbol{R} = \boldsymbol{R}' - \boldsymbol{R} + \Delta\boldsymbol{T}$. In order to disentangle the effect of the JT distortion from other lattice distortions, the TB model parameters are obtained from two crystal structures:

TABLE I. Wyckoff positions of the R = La, Pr, Nd, Sm, Eu, Gd site ($4c$) and the two inequivalent oxygen sites O1 ($4c$) and O2 ($8d$) in the room-temperature *Pbnm* experimental structures (Expt.), taken from Refs. [35,43,44] and described in Fig. 3, and their decomposition into the unit-cell volume preserving structures with only the Q^x distortion mode (JT). Mn cations are at the high-symmetry site ($4b$) with Wyckoff positions ($\frac{1}{2}$,0,0).

		Wyckoff Positions	
		Expt.	JT
LaMnO₃	La	(0.9937, 0.0435, ¼)	(0.0, 0.0, ¼)
	O1	(0.0733, 0.4893, ¼)	(0.0, 0.5, ¼)
	O2	(0.7257, 0.3014, 0.0385)	(0.7635, 0.2636, 0.0)
PrMnO₃	Pr	(0.9911, 0.0639, ¼)	(0.0, 0.0, ¼)
	O1	(0.0834, 0.4819, ¼)	(0.0, 0.5, ¼)
	O2	(0.7151, 0.3174, 0.0430)	(0.7662, 0.2662, 0.0)
NdMnO₃	Nd	(0.9886, 0.0669, ¼)	(0.0, 0.0, ¼)
	O1	(0.0878, 0.4790, ¼)	(0.0, 0.5, ¼)
	O2	(0.7141, 0.3188, 0.0450)	(0.7664, 0.2665, 0.0)
SmMnO₃	Sm	(0.9850, 0.0759, ¼)	(0.0, 0.0, ¼)
	O1	(0.0970, 0.4730, ¼)	(0.0, 0.5, ¼)
	O2	(0.7076, 0.3241, 0.0485)	(0.7659, 0.2658, 0.0)
EuMnO₃	Eu	(0.9841, 0.0759, ¼)	(0.0, 0.0, ¼)
	O1	(0.1000, 0.4700, ¼)	(0.0, 0.5, ¼)
	O2	(0.7065, 0.3254, 0.0487)	(0.7660, 0.2660, 0.0)
GdMnO₃	Gd	(0.9384, 0.0807, ¼)	(0.0, 0.0, ¼)
	O1	(0.1030, 0.4710, ¼)	(0.0, 0.5, ¼)
	O2	(0.7057, 0.3246, 0.0508)	(0.7651, 0.2651, 0.0)

the experimental and the purely JT Q^x mode distorted structure, defined by the projection of the differences in the Wyckoff positions of the experimental and the simple cubic perovskite structure to the JT Q^x mode (see Table I). We note that in this study we use the room-temperature crystal structures [35,43,44] to maintain a consistent reference for all members of the R series given the available experimental data. Therefore, the results for LaMnO₃ will differ from those in Ref. [28], where the low-temperature (4.2 K) structure from Ref. [34] was used in turn.

Two types of model parametrizations are employed, namely, model 1 and model 2. Model 1 is an effectively "noninteracting" case, in which the $\hat{H}_{\text{el-el}}$ term is neglected with the purpose of exploring how the more sophisticated beyond-PBE treatment of the XC kernel affects the hopping, JT- and GFO-distortion related parameters. Model 2 is an alternative way, involving an explicit treatment of $\hat{H}_{\text{el-el}}$ in the model Hamiltonian within the mean-field approximation. This allows us to obtain estimates of the corresponding on-site interaction parameter by keeping the PBE on-site model parameters as reference (see below).

In the following, for completeness, the considered TB model parameters are briefly described. For more details on the practical use of the VASP2WANNIER90 interface, as well as the derivation of the model parameters used in this study, we refer to Ref. [28].

A. Hopping parameters

The kinetic energy is parametrized with seven parameters: four hopping amplitudes and the JT distortion induced splitting in the nearest-neighbor hopping matrix, all evaluated in the purely JT Q^x mode distorted structure, and two spin-dependent reduction parameters of the hoppings due to the GFO distortion. For notation clarity, we set the origin ($\boldsymbol{R} = \boldsymbol{0}$) at one of the Mn sites and align the x and y Cartesian axes with the direction of the long and short Mn-O bonds of the JT Q^x mode, respectively. The vectors $\hat{\boldsymbol{x}},\hat{\boldsymbol{y}},\hat{\boldsymbol{z}}$ correspond to the nearest-neighbor spacing of the Mn sites along the respective axes [28].

Nearest-neighbor hopping amplitudes t^{ss} between sites within the FM planes ($t^{\uparrow\uparrow},t^{\downarrow\downarrow}$,$s$ is a local spin index) are obtained as $t^{ss} = (h_{11}^x - 3h_{22}^x)/2$. The hopping parameter between sites with antiparallel spin alignment is calculated as $t^{ss'} = (t^{\uparrow\uparrow} + t^{\downarrow\downarrow})/2$. The corresponding hopping matrices are then expressed as $\mathbf{t}^{ss'}(\pm\hat{z}) = -t^{ss'}(\mathbf{I} + \boldsymbol{\tau}^z)/2$ and $\mathbf{t}^{ss}(\pm\hat{x}) = -t^{ss}(2\,\mathbf{I} - \sqrt{3}\,\boldsymbol{\tau}^x - \boldsymbol{\tau}^z)/4$, where $\mathbf{I}$ is the unity matrix. Here and in the following, the matrices along $\pm\hat{y}$ are simply obtained by the relevant symmetry transformation of the matrices along $\pm\hat{x}$.

The JT distortion induces a splitting between the nondiagonal elements of the nearest-neighbor hopping matrix. We model it as $\Delta\mathbf{t}^{ss}(\pm\hat{x}) = i\,\tilde{\lambda}\,Q_{\boldsymbol{R}}^x\boldsymbol{\tau}^y$, where the parameter $\tilde{\lambda}$ is obtained as $\tilde{\lambda} = \sum_s (h_{12}^x - h_{21}^x)^s/(4Q^x)$.

The second-nearest neighbor hopping t^{xy} and the second-nearest neighbor hopping along the x,y,z crystal axes t^{2z} are obtained as $t^{xy} = -\sum_s (h_{11}^{xy})^s/2$ and $t^{2z} = -\sum_s (h_{11}^{2z})^s/2$. While the hopping matrices related to t^{2z} have the same form as those of t^{ss}, the second-nearest-neighbor hopping matrices are expressed via $\mathbf{t}(\pm\hat{x} \pm \hat{z}) = t^{xy}(\mathbf{I} - \sqrt{3}\,\boldsymbol{\tau}^x + \boldsymbol{\tau}^z)$ and $\mathbf{t}(\pm\hat{x} \pm \hat{y}) = t^{xy}(\mathbf{I} - 2\,\boldsymbol{\tau}^z)$.

In GFO distorted structures, all hopping matrices are scaled by a spin-dependent reduction factor $(1 - \eta_t^s)$, where $\eta_t^s = 1 - t_{(Pbnm)}^{ss}/t^{ss}$. The hopping parameter $t_{(Pbnm)}^{ss}$ is obtained analogously to the t^{ss} defined above but in the experimental crystal structure.

B. On-site parameters

The Hund's rule coupling strength is calculated in the experimental *Pbnm* structure from the orbitally averaged spin splitting of the diagonal on-site MLWF matrix elements: $J_{\text{H}} = -\sum_{a,s} \text{sgn}(s)(h_{aa}^0)^s/4$, with $\text{sgn}(s) = +1/-1$ for $s = \uparrow/\downarrow$.

The spin-dependent JT coupling parameter is determined from the eigenvalue splitting of the on-site MLWF matrix as $\lambda^s = \Delta\varepsilon^s/(2|Q^x|)$, where $\Delta\varepsilon$ is evaluated as $\Delta\varepsilon = [(h_{11}^0 - h_{22}^0)^2 + (2h_{12}^0)^2]^{1/2}$ in the JT Q^x mode distorted structure.

Similar to the hoppings, the JT coupling parameters λ^s are reduced in the GFO distorted structure by a factor of $(1 - \eta_\lambda)$, where $\eta_\lambda = 1 - (\Delta\varepsilon_{(Pbnm)}^\uparrow/|\boldsymbol{Q}|)/(\Delta\varepsilon^\uparrow/Q^x)$, with $|\boldsymbol{Q}| = \sqrt{(Q^x)^2 + (Q^z)^2}$.

C. Interaction parameters

As it was shown in Ref. [28], the U_{W} interaction parameter can be parametrized either by mapping the el-el interaction

on the difference between the majority and minority spin on-site matrix elements and suitably introducing an appropriate correction to the JT splitting $\Delta\lambda_{\mathrm{W}}^{(J)}$, or by mapping on the splitting between the occupied and unoccupied e_g bands with an appropriate correction to the Hund's coupling $\Delta J_{\mathrm{W}}^{(\lambda)}$. Here, we use the latter approach, which is described as follows.

The effective Hubbard parameter $U_{\mathrm{W}}^{(\lambda)}$ in the MLWF basis is determined as a correction to the JT induced gap (controlled by $\lambda^{\uparrow}$) in the noninteracting (PBE) case. It is calculated as $U_{\mathrm{W}}^{(\lambda)} = (\Delta\varepsilon^{\uparrow} - \Delta\varepsilon_{(\mathrm{PBE})}^{\uparrow})/\Delta n^{\uparrow}$, where $\Delta\varepsilon^{\uparrow}$ is the eigenvalue splitting of the Hamiltonian on-site matrix for a particular beyond-PBE treatment of the XC functional, $\Delta\varepsilon_{(\mathrm{PBE})}^{\uparrow}$ is its corresponding value at the PBE level, and $\Delta n^{\uparrow}$ is the eigenvalue splitting of the majority occupation matrix in the MLWF basis (all evaluated in the experimental $Pbnm$ structure). The observation that both the on-site part of the Hamiltonian and the occupation matrix can be diagonalized by the same unitary transformation was employed in the formulation.

Since the correlation-induced increase of the spin splitting is only partially covered by the one-parameter TB el-el term $U_{\mathrm{W}}^{(\lambda)}$, it can be corrected by introducing an empirical correction to the Hund's rule coupling: $\Delta J_{\mathrm{W}}^{(\lambda)} = J_{\mathrm{H}} - J_{\mathrm{H(PBE)}} - U_{\mathrm{W}}^{(\lambda)}/4$.

IV. METHODOLOGY: *Ab initio* CALCULATIONS

Spin polarized DFT calculations were performed using the Vienna *ab initio* simulation package (VASP) [52,53], without inclusion of spin-orbit coupling. Three types of XC functional treatment were employed: (1) the standard GGA with the parametrization of Perdew-Burke-Ernzerhof (PBE) [54]; (2) the screened hybrid DFT following the recipe of Heyd, Scuseria, and Ernzerhof (HSE) [55,56], involving the inclusion of 1/4 of the exact Hartree-Fock exchange in the PBE XC functional; and (3) the GW method [57], where the XC contributions are directly accounted for from the self-energy. We have adopted a single shot G_0W_0 procedure which, at a relatively moderate computational cost, generally leads to a significant improvement of the electronic properties with respect to standard DFT and hybrid functionals. Wave functions of the converged PBE calculation were used as a starting point in the evaluation of the Green's function G_0 and the fixed screened exchange W_0 [58,59].

The one-particle Kohn-Sham orbitals are computed using projected-augmented-wave (PAW) pseudopotentials [60,61], with the rare-earth f states frozen in the core (except for La). The $3s$ and $3p$ semicore states of Mn, as well as the $5s$ and $5p$ semicore states of R, were treated as valence, except for Eu and Gd where the $5s$ semicore states are excluded from the valence. For oxygen we have used the soft potential. Integrations in reciprocal space were carried out over a regular Γ-centered $6 \times 6 \times 4$ k-point mesh, except for G_0W_0 where a reduced setting of $4 \times 4 \times 4$ was adopted. The plane-wave energy cutoff was set to 400 eV for PBE and G_0W_0. After testing the influence of the energy cutoff on the HSE tight-binding parameters, a value of 300 eV was used in all HSE calculations to reduce the computational cost. The total number of bands was increased to 320 in the G_0W_0 runs. This value leads to sufficiently well converged band gap (within 0.1–0.2 eV)

but a larger value would be needed to better describe the highest unoccupied e_g manifold. Unfortunately, the inclusion of a larger number of bands would result in a prohibitive computational cost.

Ground-state electronic, optical, and magnetic properties were calculated for the experimental $Pbnm$ structure in the A-AFM order. By mapping the total-energy differences among different magnetic configurations to the Heisenberg Hamiltonian, exchange coupling parameters were evaluated within the HSE approach. With the so determined exchange parameters, an estimate for the Néel temperature was computed via Monte Carlo simulations (MC), employing the Metropolis algorithm [62] and using the Mersenne twister for the random number generation [63]. Conceptually and computationally challenging quantum spin fluctuations were not considered, expected to introduce only small corrections due to the relatively large value of the Mn^{3+} spin ($S = 2$). Finally, the TB parameters were extracted from the Hamiltonian matrix elements in the basis of the MLWFs, constructed from the *ab initio* wave functions in the A-AFM experimental and JT Q^x mode structures with the VASP2WANNIER90 interface [28]. For practical reasons, the f states of La were pushed away from the Mn e_g energy window in the PBE calculations by applying $U = 10$ eV, following the recipe of Dudarev *et al.* [51].

V. RESULTS AND DISCUSSION

In this section we present the outcomes of the combined *ab initio* and model Hamiltonian analysis. First we discuss the ground-state electronic structure, MLWFs, and dielectric properties as derived from the *ab initio* PBE, HSE, and G_0W_0 calculations. Then we will focus on the detailed explanation of the origin of the A-type AFM ordering by mapping the HSE total energies onto a Heisenberg Hamiltonian and computing the ordering temperature T_{N} from Monte Carlo simulations. Finally, an extended section will be dedicated to the TB results.

A. Electronic and dielectric properties

Figures 4(a)–4(c) depict the calculated band structures at the PBE, HSE, and G_0W_0 level, respectively, for $R\mathrm{MnO_3}$ ($R =$ La, Pr, Nd, Sm, Eu, and Gd) along with the corresponding characteristic MLWFs bands of predominantly e_g character. It is seen that upon R substitution, the features of the e_g character bands do not exhibit substantial differences. Consequently, the electronic properties, including screening effects, could be expected to remain almost unchanged over the series. The band structures depict an insulating state with an indirect energy gap. As a representative example of all compounds in the series, we show in Figs. 4(d)–4(f) the band structure and associated projected density of states (PDOS) of $Pr\mathrm{MnO_3}$. The PDOS is shown for the Mn e_g/t_{2g} and O p character. The overall bonding picture resembles closely the one of $La\mathrm{MnO_3}$ [26–28]: the indirect band gap is opened between the lower-lying e_g states, there is a strong hybridization between Mn d and O p states, and an appreciable intermixing between Mn e_g and t_{2g} states is observed, in particular around the band gap.

The band gaps of $R\mathrm{MnO_3}$ and the local magnetic moments at the Mn^{3+} sites with the different levels of exchange-correlation treatment are presented in Table II. The magnetic
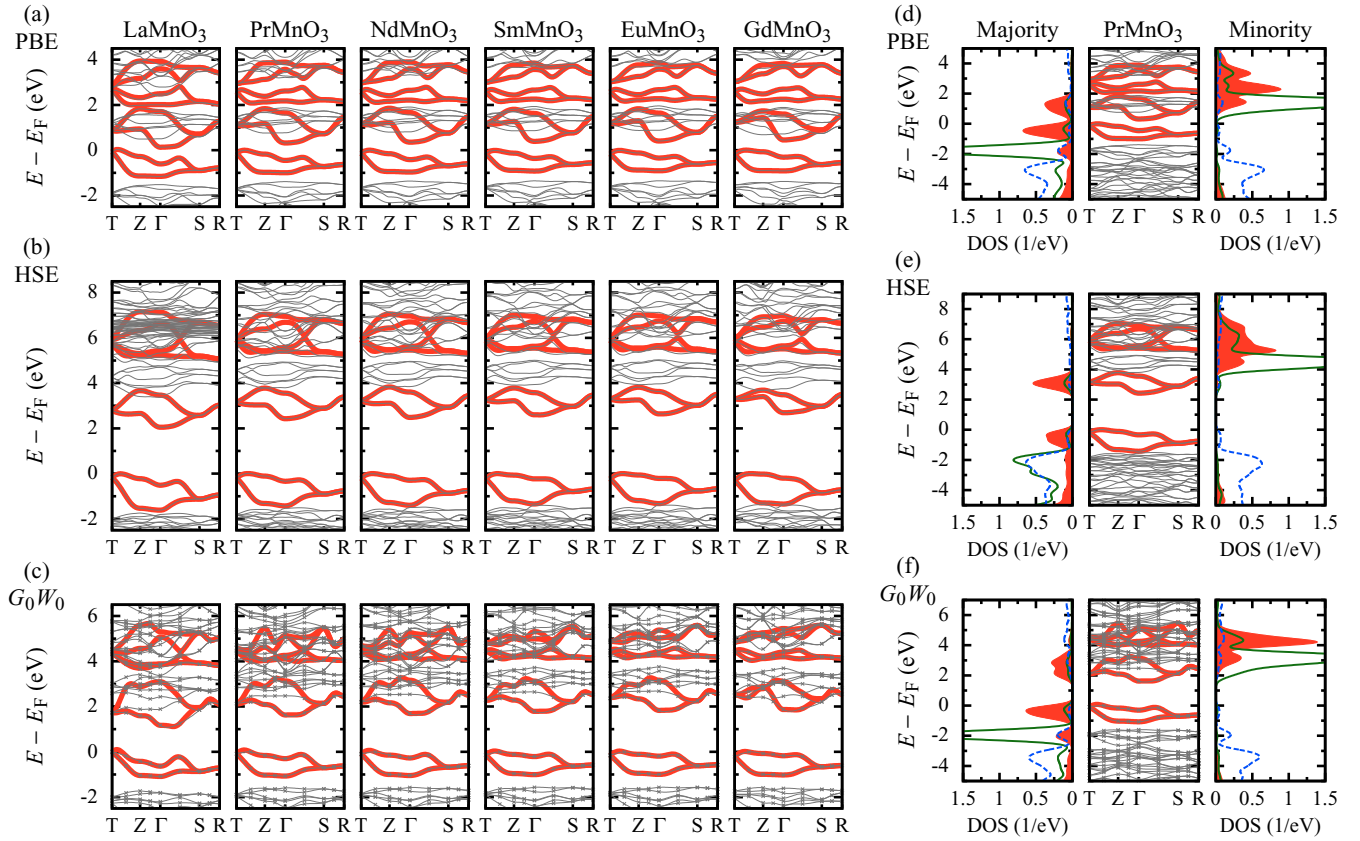
FIG. 4. The *ab initio* (thin lines) and e_g character MLWF (thick lines) band structure of $R\mathrm{MnO_3}$ (R = La, Pr, Nd, Sm, Eu, Gd) for (a) PBE, (b) HSE, and (c) G_0W_0. Band structure and associated normalized projected density of states (PDOS) for $\mathrm{PrMnO_3}$: Mn e_g (filled areas under curve), Mn t_{2g} (solid lines), and O p (dashed line) for (d) PBE, (e) HSE, and (f) G_0W_0. Left/right PDOS correspond to local majority/minority Mn sites while O p PDOS is calculated as an average over all O sites.

moment at the $\mathrm{Mn^{3+}}$ sites remains basically unaltered along the R series, while a general trend of the band gap increase from La to Gd is seen at all XC levels. The overall increment in the direct band gap is of about 0.4 and 0.5 eV at the HSE and G_0W_0 level, respectively, and in the indirect band gap of about 0.7 eV in both cases. The experimental data, not available for $\mathrm{EuMnO_3}$, do not show a clear trend but are generally in line with the G_0W_0 expectations for the direct band gap. Although still capturing the insulating nature, PBE results in much too small values of the band gap as expected. On the other hand, the HSE values appear too overestimated. This is likely due to the amount of exact exchange incorporated in the HSE functional. In the present study, we have used the standard 0.25 compromise [55,56]. However, recent systematic studies on the role of the mixing parameter on the physical properties of perovskites have indicated that a lower fraction should be used (0.1–0.15), to achieve a more consistent picture [26,29].

The dielectric function measured in an energy range 0.5–5.5 eV shows two intensive, broad optical features peaked at approximately 2 and 4.5 eV for $\mathrm{LaMnO_3}$ (Fig. 5). For the other $R\mathrm{MnO_3}$ compounds, the intensive broad peak is positioned at ≈ 2.2 eV. While the authors in Refs. [76–78] assign the peaks to d-d charge-transfer excitations, the authors of Ref. [23] argue that the peaks are due to the interplay of both p-d and d-d transitions. These experimental results are in line with the measurements of Kim *et al.* [22]. The G_0W_0 results

capture well the double peak structure, but the intensity of the first peak and the zero frequency value of the real part of the dielectric function ϵ_1, which identifies the macroscopic dielectric constant ϵ_∞, is about two times larger than the experimental one. A better agreement with experiment could possibly be achieved by increasing the number of bands, the k-points sampling, and by treating the screened exchange at beyond-PBE level (i.e., within a fully self-consistent GW framework) but this is beyond the scope of the present study (the corresponding calculation would be computationally very demanding) [79] and will be addressed in a future paper [80].

B. Magnetic properties

We further analyze the magnetic properties of the $R\mathrm{MnO_3}$ compounds in terms of the exchange interactions J_{ij} between sites i and j, obtained by mapping the total energy of different magnetic configurations on the Heisenberg Hamiltonian,

$$H = -\frac{1}{2} \sum_{i \neq j} J_{ij} \, \boldsymbol{S}_i \cdot \boldsymbol{S}_j, \tag{5}$$

for $|\boldsymbol{S}_i| = |\boldsymbol{S}_j| = 2$, with positive and negative values of J_{ij} corresponding to FM and AFM coupling, respectively. In the four formula unit cell there are three exchange interactions that can be extracted: the in-plane nearest neighbor J_x, the out-of-plane nearest neighbor J_z, and second nearest neighbor J_{xz};

TABLE II. The values of indirect (smallest direct) band gap and magnetic moment at the Mn^{3+} sites of RMnO$_3$ series.

	Band gap (eV)			
	PBE	HSE	G_0W_0	Expt.
LaMnO$_3$	0.13 (0.56)	2.06 (2.48)	1.15 (1.49)	1.7,[a] 1.9,[b] 2.0[c]
PrMnO$_3$	0.32 (0.72)	2.43 (2.74)	1.63 (1.81)	1.75,[d] 2.0[e]
NdMnO$_3$	0.36 (0.74)	2.49 (2.78)	1.70 (1.86)	1.75,[d] 1.78[f]
SmMnO$_3$	0.40 (0.75)	2.61 (2.80)	1.79 (1.92)	1.82[f]
EuMnO$_3$	0.42 (0.75)	2.65 (2.85)	1.84 (1.96)	
GdMnO$_3$	0.45 (0.75)	2.70 (2.89)	1.87 (1.99)	2.0,[g] 2.9[h]
	Magnetic moment (μ_B)			
	PBE	HSE	G_0W_0	Expt.
LaMnO$_3$	3.49	3.72	3.40	3.4,[i] 3.87,[j] 3.65[k]
PrMnO$_3$	3.49	3.71	3.40	3.5[l]
NdMnO$_3$	3.49	3.71	3.40	3.22[m]
SmMnO$_3$	3.49	3.71	3.40	3.3[n]
EuMnO$_3$	3.49	3.71	3.40	
GdMnO$_3$	3.47	3.70	3.38	

[a]Reference [64].
[b]Reference [65].
[c]Reference [66].
[d]Reference [67].
[e]Reference [68].
[f]Reference [69].
[g]Reference [70].
[h]Reference [71].
[i]Reference [72].
[j]Reference [73].
[k]Reference [74].
[l]Reference [17].
[m]Reference [14].
[n]Reference [75].

where the subscripts are a shorthand notation of the direction connecting the sites in the pseudocubic axes frame [see Fig. 6(a)]. Determining interactions between further neighbors would require a larger supercell. While often only the first two parameters are taken into consideration [81,82], it was reported that the A-AFM order in LaMnO$_3$ can be seen as a competition between a weakly FM J_z and a weakly AFM J_{xz} coupling [83]. As it was discussed previously, simple treatments of the exchange-correlation functional (such as PBE) were shown to be inadequate in providing a good prediction of the magnetic properties/interactions for perovskites and in general for transition-metal oxides [21,84]. Although the exchange interactions in LaMnO$_3$ calculated using hybrid functionals were found to be largely dependent on the choice of the particular hybrid functional, the A-AFM order is consistently predicted to be the magnetic ground state [81]. We therefore base our analysis on the total energies calculated using the HSE functional, that has been already employed successfully in combination with the Monte Carlo method to predict the magnetic ordering temperature in transition-metal perovskites [85].

We also note that a recent study has shown that the magnetic properties of the later members of the manganite series ($R =$ Tb to Lu) are not well described by a standard Heisenberg model with pairwise bilinear interactions, and that additional
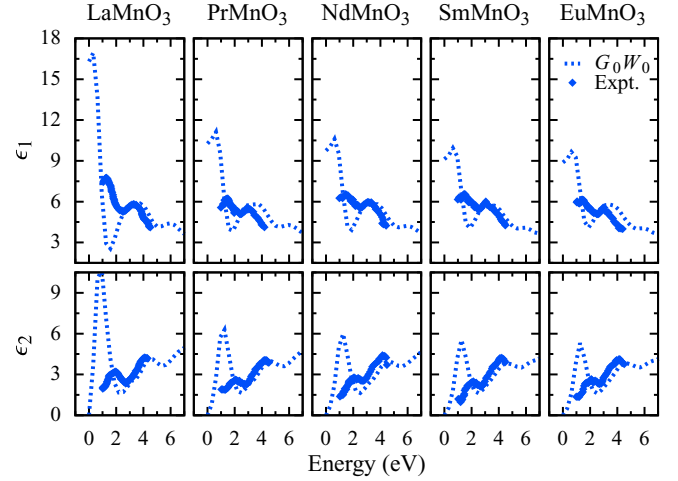

FIG. 5. The real (ϵ_1) and imaginary (ϵ_2) part of the dielectric function. The dotted lines indicate the G_0W_0 data and the filled diamonds correspond to the experimental data taken from Ref. [23].

biquadratic or four-spin ring exchange interactions need to be considered [86]. However, for the larger rare-earth cations considered in this study, the Heisenberg model is expected to provide a sufficiently accurate description.

The total energy was calculated for the five symmetry inequivalent magnetic configurations compatible with the unit cell. These include the ferromagnetic order (B); the three distinct antiferromagnetic configurations A-AFM (A), C-AFM (C), and G-AFM (G); and the single nondegenerate ferrimagnetic state (Fi), as depicted in Fig. 6(a). For brevity, the shorthand notation in parentheses [87] will be used in this section to denote the total energies of the corresponding magnetic configuration. These, by using Eq. (5), are expressed as

$$E_A = E_0 - 32J_x + 16J_z + 64J_{xz}, \quad (6a)$$

$$E_B = E_0 - 32J_x - 16J_z - 64J_{xz}, \quad (6b)$$

$$E_C = E_0 + 32J_x - 16J_z + 64J_{xz}, \quad (6c)$$

$$E_G = E_0 + 32J_x + 16J_z - 64J_{xz}, \quad (6d)$$

$$E_{Fi} = E_0, \quad (6e)$$

where E_0 is a fitting constant in unit of energy that should correspond to the energy of the paramagnetic state. The total energies relative to E_A are plotted in Fig. 6(b). For all members of the R series, the A ordering yields the lowest energy among the five considered magnetic configurations. While the difference in the total energy from the C or G orders on one side to the A or B orders on the other side are relatively large in the case of LaMnO$_3$, these differences decrease consistently towards GdMnO$_3$, following the trend of decreasing T_N. We note that ($E_C - E_A$) does not differ from 2($E_{Fi} - E_A$) by more than 2 meV.

The solution to the overdetermined system of equations composed by Eqs. (6a)–(6e) is obtained by a linear least-squares fit and the resulting exchange interaction parameters J_x, J_z, and J_{xz} are shown in Fig. 6(c). The in-plane J_x interaction is FM throughout the whole R series, monotonously and strongly decreasing from La to Gd. The out-of-plane J_z
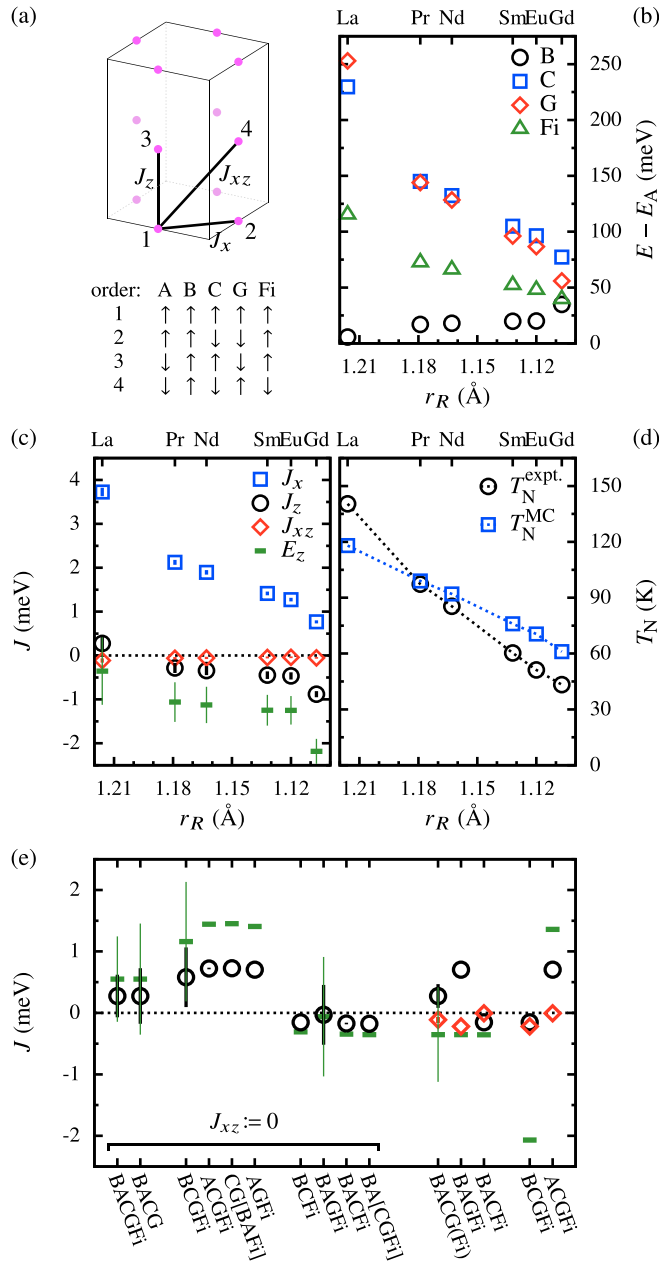
FIG. 6. (a) Schematic representation of the exchange interactions J_x, J_z, and J_{xz} in the unit cell of RMnO$_3$, together with the spin orientations in the A, B, C, G, and Fi magnetic configurations. (b) The total energy of the different magnetic configurations relative to the A ordering. (c) Exchange interactions calculated by linear least-squares fit of Eqs. (6a)–(6e) and the out-of-plane interlayer interaction energy $E_z = 2J_z + 8J_{xz}$. Errors on the estimation of the corresponding parameter are shown as vertical bars. (d) The Néel temperature, experimental $T_N^{\text{expt.}}$ [8] and calculated T_N^{MC} via MC simulations using the exchange interactions shown in (c). (e) J_z, J_{xz}, and E_z in LaMnO$_3$ for different sets of magnetic configurations. For sets yielding identical values of J_z, we adopt a notation of choose one from the list in square brackets. The BACG(Fi) data depicts both BACGFi (with error bars) and BACG (without error bars). Legend is identical to (c).

interaction exhibits a similar trend, however, the weakly FM J_z for R = La becomes weakly AFM from R = Pr on. The

stability of A order is finally determined by the out-of-plane interaction energy $E_z = 2J_z + 8J_{xz}$ being negative for all members of R series, including La. There, however, the error on the estimation of E_z is large enough to reach the FM region. By employing the Monte Carlo method, the exchange interaction parameters are used to calculate the Néel temperature presented in Fig. 6(d), generally leading to very good agreement with the experimental values [8]. By comparing Fig. 3 with Fig. 6, our results indicate that the decrease of T_N from La to Gd should be attributed to the gradual reduction of J_x which is associated with the progressive decrease of the Mn-O-Mn in-plane bond angle ϕ_{ab} over the series, in accordance with the conclusions of Kimura *et al.* [8]. In addition, it is important to note that the strong reduction of J_x over the series is a clear indication of the gradual destabilization of the A-type ordering. For Gd, in fact, the in-plane and out-of-plane exchange interactions become very similar, suggesting an incipient transition towards a different type of magnetic ordering, in line with the experimental phase diagram [8,48].

We note that for the case of LaMnO$_3$ it is of particular importance to include the out-of-plane second-neighbor interaction in the model. Furthermore, the calculated exchange interactions are particularly sensitive to the choice of the subset M of magnetic configurations to include in the system of equations [see Fig. 6(e)]. By setting $J_{xz} = 0$ and operating Eqs. (6a)–(6e), it is easy to show that J_z can be calculated from any of the following expressions:

$$J_z = \frac{1}{32} \begin{cases} (E_A + E_G - 2E_{Fi}): & \{AGFi\} \in M, \quad (7a) \\ (2E_{Fi} - E_B - E_C): & \{BCFi\} \in M, \quad (7b) \\ (E_A - E_B): & \{AB\} \in M, \quad (7c) \\ (E_G - E_C): & \{CG\} \in M. \quad (7d) \end{cases}$$

For R = Pr–Gd, the J_z calculated from Eqs. (7a)–(7d) is always negative, whereas in LaMnO$_3$ its sign becomes positive when using Eqs. (7a) and (7d). Using all five energy points (BACGFi) the linear least-squares fit to Eqs. (6a)–(6e) yields a FM J_z whose magnitude is the average obtained from Eqs. (7a) and (7b), but with an error in the estimation of the parameter large enough to turn it AFM. An out-of-plane FM coupling is obtained when either AGFi or CG are present in M, which is inconsistent with the experimentally observed magnetic ground state (sets BCGFi, ACGFi, BCG, ACG, CGFi, and AGFi). Conversely, when either BCFi or AB are present in M (sets BCFi, BAGFi, BACFi, BAC, BAG, and BAFi), the system of equations yields a negative J_z in agreement with experiments. However, that would be the equivalent of removing inconvenient data to adjust it to a desired outcome, when actually these inconsistencies can be ascribed to the fact that without J_{xz} the expansion of the Heisenberg Hamiltonian is incomplete. Including J_{xz} as a third interaction parameter, only Eqs. (7a) and (7b) hold. The out-of-plane magnetic coupling is driven by the previously defined interaction energy E_z, which can be regarded as the effective out-of-plane exchange interaction. As shown in Fig. 6(e), provided that both A and B are present in M, E_z is not only negative but rather insensitive to the configuration of the subset, in spite of
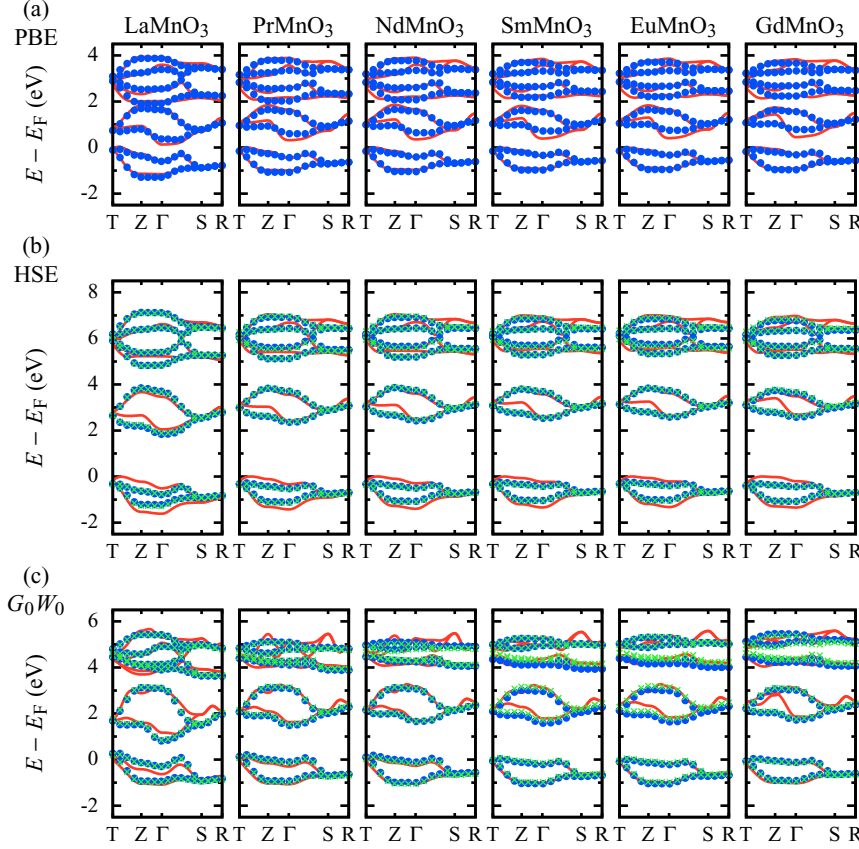
FIG. 7. The TB bands calculated according to model 1 (filled circles) and model 2 (crosses) with the MLWFs bands (solid lines) in the background.

the pronounced differences obtained in the particular values of J_z and J_{xz}. This is so because E_z is calculated as

$$E_z = \frac{1}{16} \begin{cases} (E_A - E_B): & \{AB\} \in M, & \text{(8a)} \\ (4E_{Fi} - 2E_B - E_C - E_G): & A \notin M, & \text{(8b)} \\ (2E_A + E_C + E_G - 4E_{Fi}): & B \notin M. & \text{(8c)} \end{cases}$$

When either A or B are not members of M, Eqs. (8b) and (8c) would be equivalent to Eq. (8a) if the following identity, stemming from Eqs. (6a)–(6e), is verified: $E_A + E_B + E_C + E_G = 4E_{Fi}$. However, not only is the Heisenberg model itself an approximation, but also the *ab initio* total energies are not exempt from errors due to various approximations affecting the calculations. Since the out-of-plane exchange parameters are of comparable magnitude to these errors (in the order of meV), minor deviations in the previous equality led to the observed large differences in J_z, J_{xz}, and E_z. This is the reason why it is advisable and often necessary to extract the exchange parameters from as large sets of magnetic configurations as possible.

C. Tight binding

We remind that we performed two types of TB parametrizations: model 1 and model 2. In model 1, the term $\hat{H}_{\text{el-el}}$ is not considered; the el-el interaction is implicitly accounted for in the HSE and G_0W_0 hopping, JT- and GFO-induced parameters, which will differ from the corresponding PBE values. In model 2, the modifications due to the beyond-PBE

methods are treated as a perturbation to the "noninteracting" PBE description by explicitly considering the $\hat{H}_{\text{el-el}}$ term in the mean-field approximation. The band structures obtained with these sets of TB parameters compared with the corresponding MLWFs bands are shown in Fig. 7. The individual TB parameters are shown in Figs. 8 and 9 and are presented in detail in Table III.

In general, very good qualitative agreement can be seen between the features of the TB and MLWF bands (Fig. 7). Moreover, almost no difference is found between the bands calculated with the TB parameters using model 1 and model 2. While the match for LaMnO$_3$ at the PBE level (for which the procedure was originally developed in Ref. [38]) is very good, deviations for the lowest unoccupied e_g character band increase along the R series. This is not surprising considering that the progressively stronger GFO distortion makes the assumption of the individual structural distortions acting independently less valid. Nevertheless, the root mean square and maximum deviation between the band and k-point averaged sets of eigenvalues for the TB and MLWF bands are typically around very acceptable values: 0.15 and 0.5 eV, respectively. The quantitative deviations observed in the G_0W_0 local minority bands can be, on the other hand, attributed to difficulties in achieving well-converged results at the G_0W_0 level.

In the following we analyze in detail how the hopping and on-site TB parameters are affected along the R series at different levels of the XC functional treatment.

Regarding the hopping parameters (Fig. 8 and Table III), the nearest-neighbor hoppings $t^{\uparrow\uparrow}$ and $t^{\downarrow\downarrow}$ (calculated using

TABLE III. The tight-binding parameters. The hopping parameters $t^{\uparrow\uparrow}$ and $t^{\downarrow\downarrow}$ for the JT structure in Fig. 8 correspond to the $t^{\uparrow\uparrow}$ and $t^{\downarrow\downarrow}$ presented in this table.

		Hopping parameters						On-site parameters				Model 2			
		$t^{\uparrow\uparrow}$ (meV)	$t^{\downarrow\downarrow}$ (meV)	$\widetilde{\lambda}$ (eV/Å)	t^{xy} (meV)	t^{2z} (meV)	$\eta_t^{\uparrow}$	$\eta_t^{\downarrow}$	J_H (eV)	$\lambda^{\uparrow}$ (eV/Å)	$\lambda^{\downarrow}$ (eV/Å)	η_λ	$\Delta\varepsilon^{\uparrow}$ (eV)	$\Delta n^{\uparrow}$	$U_W^{(\lambda)}$ (eV)	$\Delta J_W^{(\lambda)}$ (eV)
PBE	LaMnO$_3$	627	499	0.55	12	51	0.27	0.37	1.34	3.31	0.80	0.23	0.85			
	PrMnO$_3$	631	500	0.53	12	51	0.40	0.46	1.30	3.36	1.03	0.28	1.12			
	NdMnO$_3$	635	511	0.52	12	51	0.42	0.50	1.30	3.39	1.06	0.29	1.15			
	SmMnO$_3$	645	523	0.52	12	51	0.46	0.57	1.29	3.46	1.08	0.31	1.18			
	EuMnO$_3$	649	526	0.52	12	51	0.47	0.58	1.29	3.49	1.11	0.31	1.21			
	GdMnO$_3$	655	537	0.51	12	51	0.48	0.60	1.29	3.52	1.10	0.28	1.26			
HSE	LaMnO$_3$	686	551	1.36	12	51	0.18	0.42	2.44	10.49	1.02	0.16	2.96	0.87	2.42	0.50
	PrMnO$_3$	732	558	1.04	10	52	0.35	0.55	2.39	9.59	0.41	0.25	3.31	0.90	2.43	0.48
	NdMnO$_3$	743	564	1.02	10	52	0.38	0.57	2.39	9.61	0.36	0.26	3.36	0.91	2.44	0.48
	SmMnO$_3$	766	579	0.99	11	53	0.44	0.62	2.38	9.97	0.43	0.31	3.41	0.92	2.42	0.48
	EuMnO$_3$	776	583	0.96	12	53	0.45	0.63	2.38	10.03	0.38	0.32	3.45	0.92	2.43	0.48
	GdMnO$_3$	789	587	0.97	12	54	0.48	0.63	2.37	10.41	0.53	0.32	3.50	0.93	2.43	0.47
G_0W_0	LaMnO$_3$	753	462	0.74	66	78	0.20	0.57	1.83	4.86	1.18	0.10	1.46	0.61	1.00	0.24
	PrMnO$_3$	736	389	0.64	51	64	0.27	0.72	1.76	4.71	1.12	0.08	2.00	0.73	1.21	0.16
	NdMnO$_3$	732	460	0.64	36	69	0.28	0.79	1.79	4.73	1.22	0.07	2.10	0.76	1.24	0.19
	SmMnO$_3$	747	533	0.70	40	60	0.33	0.74	1.83	4.85	1.51	0.08	2.21	0.78	1.32	0.21
	EuMnO$_3$	767	556	0.71	38	54	0.35	0.75	1.85	4.95	1.47	0.09	2.27	0.79	1.35	0.22
	GdMnO$_3$	772	561	0.72	43	48	0.39	0.73	1.86	4.99	1.54	0.06	2.32	0.81	1.32	0.24

the purely JT distorted structure) exhibit a slight monotonic increase with R for PBE and HSE, which can be attributed to the unit-cell volume reduction. This trend is not followed for early R series members at G_0W_0. The deviation is not as pronounced for $t^{\uparrow\uparrow}$ as it is for $t^{\downarrow\downarrow}$, but in general, as mentioned above, results for the minority bands at G_0W_0 should be taken with much care. The increase in $t^{\uparrow\uparrow}$ from the PBE values to those at beyond PBE levels is due to the stronger hybridization with lower-lying O p states [28,50]. The strong reduction of the hopping amplitude due to the increasing GFO distortion along the R series can be seen in the plots of $t^{\uparrow\uparrow}$ and $t^{\downarrow\downarrow}$ (calculated using the $Pbnm$ structure) and in the corresponding derived reduction parameters $\eta_t^{\uparrow}$ and $\eta_t^{\downarrow}$. While the reduction is strongest at PBE, generally followed by HSE and G_0W_0 in the case of majority spin, reversed behavior can be seen for the minority spin. The decrease of the hoppings correlates with the reduction of Mn-O-Mn in-plane angle ϕ_{ab} and the Néel temperature. The further neighbor hopping parameters t^{xy} and t^{2z} remain nearly unchanged along the R series for PBE and HSE. Not much significance should be given to the irregularities observed for G_0W_0, since the notorious difficulty to properly converge the minority bands can have a very pronounced effect on these parameters. The $\widetilde{\lambda}$ parameter, controlling the JT induced splitting in the hopping matrix, is largely independent on R (except $R = $ La for HSE) and its magnitude increases from PBE through G_0W_0 to HSE, resembling the behavior of the on-site parameters $\lambda^{\uparrow}$ and J_H (see below).

The on-site TB parameters as a function of R calculated for different XC kernel treatment are presented in Fig. 9 and Table III. For completeness, the numerical values of the majority spin eigenvalue splitting $\Delta\varepsilon^{\uparrow}$ and occupation matrix splitting $\Delta n^{\uparrow}$ needed for $U_W^{(\lambda)}$ evaluation are also listed in Table III. The majority spin JT coupling strength $\lambda^{\uparrow}$ and the Hund's rule coupling strength J_H are almost constant along the R series. They also exhibit a mutually consistent qualitative increase at the HSE and G_0W_0 levels (compare with $\widetilde{\lambda}$ above), which is reflected in the TB model by an increase in the band gap ($\lambda^{\uparrow}$) and the spin splitting (J_H). The magnitude of $\lambda^{\downarrow}$ is significantly smaller than that of $\lambda^{\uparrow}$. This can be explained using the simple argument of the weaker d-p hybridization for the higher-lying minority bands [38]. The irregularities along the R series for G_0W_0 are again caused by the quality of the minority spin bands. The reduction parameter of the JT coupling strength due to the GFO distortion η^{λ} is weaker than the corresponding hopping reduction parameters ($\eta^{\uparrow}$ and $\eta^{\downarrow}$). Its relative change down the R series is comparable for PBE and HSE, while the results for G_0W_0 are almost R independent.

In order to capture both the spin splitting and the band-gap increase when using HSE and G_0W_0, a single interaction parameter $U_W^{(\lambda)}$ is not sufficient and a semiempirical correction to the Hund's coupling $\Delta J_W^{(\lambda)}$ is also needed in model 2. Here, the hopping parameters of the respective method are used, while the on-site parameters are kept fixed at their PBE values. The el-el interaction parameter $U_W^{(\lambda)}$ as a function of R can be regarded as a constant for HSE, while it exhibits a small increase in the case of G_0W_0. The value of $U_W^{(\lambda)}$ is significantly different for HSE and G_0W_0. The much larger HSE value can be a consequence of the mixing parameter used in these calculations [26,29], which consistently leads to an overestimation of the band gap (see Table II). The quantitatively less important $\Delta J_W^{(\lambda)}$ follows the same trend as $U_W^{(\lambda)}$.
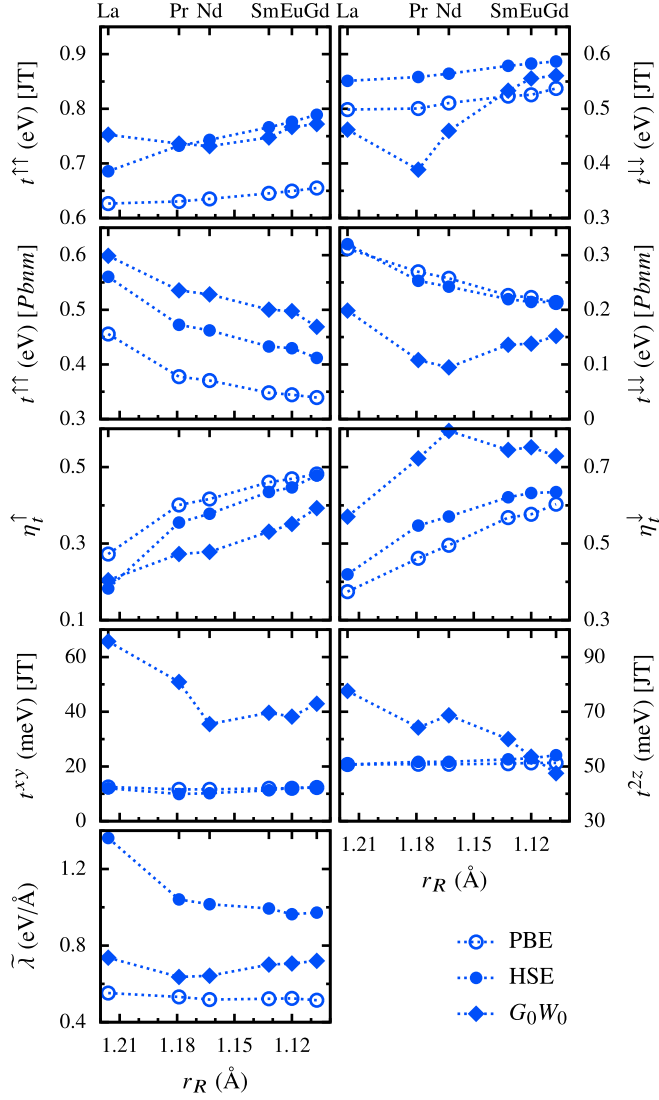
FIG. 8. Dependence of the TB hopping related model parameters on r_R. The nearest-neighbor hopping parameters $t^{\uparrow\uparrow}$ and $t^{\downarrow\downarrow}$ are shown in the JT(Q^x) and experimental *Pbnm* crystal structure, which are used to determine the GFO-induced reduction factors $\eta^{\uparrow}$ and $\eta^{\downarrow}$. Ensuing, the further neighbor hopping parameters t^{xy} and t^{2z} and the JT-induced splitting in the nondiagonal elements of the nearest-neighbor in-plane hopping matrix $\widetilde{\lambda}$ are shown.

VI. CONCLUSIONS

A combination of first-principles calculations and tight-binding (TB) model Hamiltonian via maximally localized Wannier functions (MLWFs) was applied to the parent compounds of manganites RMnO$_3$ (R = La, Pr, Nd, Sm, Eu, and Gd). The electronic and magnetic properties were studied at different levels of XC treatment.

The band structures within the same XC level exhibit similar features along the R series. The calculations show a clear trend of an increase of the electronic band gap with the decrease of the R cation radius r_R. While PBE band gaps are severely underestimated, the HSE values are overestimated likely due to the amount of the exact exchange included in the
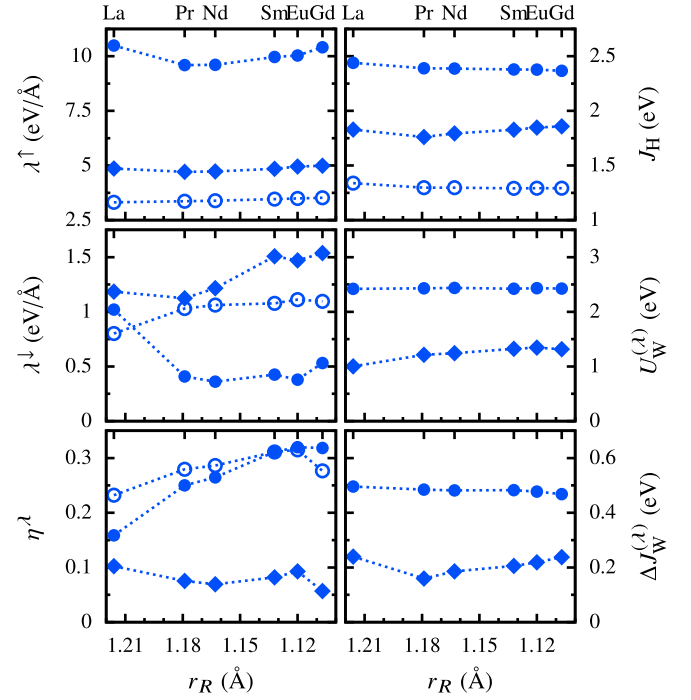

FIG. 9. Dependence of the TB on-site model parameters on r_R: JT coupling parameters $\lambda^{\uparrow}$, $\lambda^{\downarrow}$ and the GFO-induced reduction parameter of the JT coupling η^{λ}, Hund's coupling J_H, the mean-field Hubbard parameter $U_W^{(\lambda)}$, and the correction to the Hund's coupling $\Delta J_W^{(\lambda)}$. For legend see Fig. 8.

functional. The values obtained for G_0W_0 seem to be more consistent with the available experimental data. Likewise, the dielectric function calculated within G_0W_0 is in reasonable qualitative agreement with experiments but the intensity of the first peak and ϵ_∞ are significantly overestimated.

The exchange couplings obtained at the HSE level yield Monte Carlo simulated Néel temperatures that are in very good agreement with experimental observations. The weakening of the FM in-plane exchange interaction parameter with decreasing r_R is a clear indication of the destabilization of the A-type AFM order towards the E-type AFM order observed in further members of the R series. Concurrently, the effective AFM out-of-plane exchange interaction strengthens and it is only in LaMnO$_3$ where the out-of-plane anti-ferromagnetism cannot be attributed to a single exchange parameter and it is necessary to include the out-of-plane second neighbor interaction in order to stabilize the A-type AFM order.

Despite the difficulties in the disentanglement of the e_g character states mainly at the G_0W_0 level, the obtained MLWF bands are in very good agreement with the underlying *ab initio* bands. The method-derived changes in the TB parameters due to different treatments of the XC kernel has been investigated and accounted for using two parametrization models. In general, an overall consistent qualitative trend in the description of the TB parameters has been found for all the compounds down the R series at the PBE, HSE, and G_0W_0 levels. The trends in the nearest-neighbor hopping amplitudes in the *Pbnm* structure are comparable with those of the volume, tolerance

factor, Mn-O-Mn bond angles, and the Néel temperature. Another interesting result is that the JT and Hund's rule coupling strength, as well as the simple mean-field electron-electron interaction parameter, are practically R independent and can be regarded as method dependent universal constants in the $R\text{MnO}_3$ series.

[1] R. von Helmolt, J. Wecker, B. Holzapfel, L. Schultz, and K. Samwer, Phys. Rev. Lett. **71**, 2331 (1993).

[2] M. B. Salamon and M. Jaime, Rev. Mod. Phys. **73**, 583 (2001).

[3] D. Khomskii and G. Sawatzky, Solid State Commun. **102**, 87 (1997).

[4] R. Kusters, J. Singleton, D. Keen, R. McGreevy, and W. Hayes, Physica B: Condens. Matter **155**, 362 (1989).

[5] S. Jin, T. H. Tiefel, M. McCormack, R. A. Fastnacht, R. Ramesh, and L. H. Chen, Science **264**, 413 (1994).

[6] Y. Tokura, A. Urushibara, Y. Moritomo, T. Arima, A. Asamitsu, G. Kido, and N. Furukawa, J. Phys. Soc. Jpn. **63**, 3931 (1994).

[7] C. Zener, Phys. Rev. **82**, 403 (1951).

[8] T. Kimura, S. Ishihara, H. Shintani, T. Arima, K. T. Takahashi, K. Ishizaka, and Y. Tokura, Phys. Rev. B **68**, 060403 (2003).

[9] T. Goto, T. Kimura, G. Lawes, A. P. Ramirez, and Y. Tokura, Phys. Rev. Lett. **92**, 257201 (2004).

[10] T. Kimura, G. Lawes, T. Goto, Y. Tokura, and A. P. Ramirez, Phys. Rev. B **71**, 224425 (2005).

[11] M. C. Sánchez, G. Subías, J. García, and J. Blasco, Phys. Rev. Lett. **90**, 045503 (2003).

[12] W. S. Ferreira, J. Agostinho Moreira, A. Almeida, M. R. Chaves, J. P. Araújo, J. B. Oliveira, J. M. Machado Da Silva, M. A. Sá, T. M. Mendonça, P. Simeão Carvalho *et al.*, Phys. Rev. B **79**, 054303 (2009).

[13] T. Chatterji, G. J. Schneider, L. van Eijck, B. Frick, and D. Bhattacharya, J. Phys.: Condens. Matter **21**, 126003 (2009).

[14] A. Muñoz, J. A. Alonso, M. J. Martínez-Lope, J. L. García-Muñoz, and M. Fernández-Díaz, J. Phys.: Condens. Matter **12**, 1361 (2000).

[15] N. Kamegashira and Y. Miyazaki, Phys. Status Solidi A **76**, K39 (1983).

[16] B. Dabrowski, S. Kolesnik, A. Baszczuk, O. Chmaissem, T. Maxwell, and J. Mais, J. Solid State Chem. **178**, 629 (2005).

[17] J. Laverdière, S. Jandl, A. A. Mukhin, V. Y. Ivanov, V. G. Ivanov, and M. N. Iliev, Phys. Rev. B **73**, 214301 (2006).

[18] M. N. Iliev, M. V. Abrashev, J. Laverdière, S. Jandl, M. M. Gospodinov, Y.-Q. Wang, and Y.-Y. Sun, Phys. Rev. B **73**, 064302 (2006).

[19] J. S. Lee, N. Kida, S. Miyahara, Y. Takahashi, Y. Yamasaki, R. Shimano, N. Furukawa, and Y. Tokura, Phys. Rev. B **79**, 180403 (2009).

[20] A. Iyama, J.-S. Jung, E. Sang Choi, J. Hwang, and T. Kimura, J. Phys. Soc. Jpn. **81**, 013703 (2012).

[21] K. Yamauchi, F. Freimuth, S. Blügel, and S. Picozzi, Phys. Rev. B **78**, 014403 (2008).

[22] B. H. Kim and B. I. Min, Phys. Rev. B **80**, 064416 (2009).

[23] A. S. Moskvin, A. A. Makhnev, L. V. Nomerovannaya, N. N. Loshkareva, and A. M. Balbashov, Phys. Rev. B **82**, 035106 (2010).

[24] S. Dong, R. Yu, S. Yunoki, J.-M. Liu, and E. Dagotto, Eur. Phys. J. B **71**, 339 (2009).

[25] R. Choithrani, M. N. Rao, S. L. Chaplot, N. K. Gaur, and R. K. Singh, New J. Phys. **11**, 073041 (2009).

[26] J. He and C. Franchini, Phys. Rev. B **86**, 235117 (2012).

[27] J. He, M.-X. Chen, X.-Q. Chen, and C. Franchini, Phys. Rev. B **85**, 195135 (2012).

[28] C. Franchini, R. Kováčik, M. Marsman, S. Sathyanarayana Murthy, J. He, C. Ederer, and G. Kresse, J. Phys.: Condens. Matter **24**, 235602 (2012).

[29] C. Franchini, J. Phys.: Condens. Matter **26**, 253202 (2014).

[30] W.-G. Yin, D. Volja, and W. Ku, Phys. Rev. Lett. **96**, 116405 (2006).

[31] J. Rodríguez-Carvajal, M. Hennion, F. Moussa, A. H. Moudden, L. Pinsard, and A. Revcolevschi, Phys. Rev. B **57**, R3189 (1998).

[32] T. Chatterji, F. Fauth, B. Ouladdiaf, P. Mandal, and B. Ghosh, Phys. Rev. B **68**, 052406 (2003).

[33] X. Qiu, T. Proffen, J. F. Mitchell, and S. J. L. Billinge, Phys. Rev. Lett. **94**, 177203 (2005).

[34] J. B. A. A. Elemans, B. Van Laar, K. R. Van Der Veen, and B. O. Loopstra, J. Solid State Chem. **3**, 238 (1971).

[35] P. Norby, I. G. Krogh Andersen, E. Krogh Andersen, and N. H. Andersen, J. Solid State Chem. **119**, 191 (1995).

[36] P. M. Woodward, Acta Crystallogr., Sect. B: Struct. Sci. **53**, 32 (1997).

[37] K. Momma and F. Izumi, J. Appl. Crystallogr. **44**, 1272 (2011).

[38] R. Kováčik and C. Ederer, Phys. Rev. B **81**, 245108 (2010).

[39] Y. Murakami, J. P. Hill, D. Gibbs, M. Blume, I. Koyama, M. Tanaka, H. Kawata, T. Arima, Y. Tokura, K. Hirota *et al.*, Phys. Rev. Lett. **81**, 582 (1998).

[40] J. Kanamori, J. Appl. Phys. **31**, S14 (1960).

[41] E. Pavarini and E. Koch, Phys. Rev. Lett. **104**, 086402 (2010).

[42] O. Sikora and A. M. Oleś, Acta Phys. Pol. B **34**, 861 (2003).

[43] J. A. Alonso, M. J. Martínez-Lope, M. T. Casais, and M. T. Fernández-Díaz, Inorg. Chem. **39**, 917 (2000).

[44] T. Mori, N. Kamegashira, K. Aoki, T. Shishido, and T. Fukuda, Mater. Lett. **54**, 238 (2002).

[45] R. D. Shannon, Acta Crystallogr., Sect. A: Cryst. Phys., Diffr., Theor. Gen. Crystallogr. **32**, 751 (1976).

[46] V. M. Goldschmidt, Naturwissenschaften **14**, 477 (1926).

[47] J.-S. Zhou and J. B. Goodenough, Phys. Rev. B **68**, 054403 (2003).

[48] J.-S. Zhou and J. B. Goodenough, Phys. Rev. Lett. **96**, 247202 (2006).

[49] C. Ederer, C. Lin, and A. J. Millis, Phys. Rev. B **76**, 155105 (2007).

[50] R. Kováčik and C. Ederer, Phys. Rev. B **84**, 075118 (2011).

[51] S. L. Dudarev, G. A. Botton, S. Y. Savrasov, C. J. Humphreys, and A. P. Sutton, Phys. Rev. B **57**, 1505 (1998).

[52] G. Kresse and J. Hafner, Phys. Rev. B **48**, 13115 (1993).

[53] G. Kresse and J. Furthmüller, Comput. Mater. Sci. **6**, 15 (1996).

[54] J. P. Perdew, K. Burke, and M. Ernzerhof, Phys. Rev. Lett. **77**, 3865 (1996).

[55] J. Heyd, G. E. Scuseria, and M. Ernzerhof, J. Chem. Phys. **118**, 8207 (2003).

[56] J. Heyd, G. E. Scuseria, and M. Ernzerhof, J. Chem. Phys. **124**, 219906 (2006).

[57] L. Hedin, Phys. Rev. **139**, A796 (1965).

[58] J. Paier, M. Marsman, and G. Kresse, Phys. Rev. B **78**, 121201(R) (2008).

[59] C. Franchini, A. Sanna, M. Marsman, and G. Kresse, Phys. Rev. B **81**, 085213 (2010).

[60] P. E. Blöchl, Phys. Rev. B **50**, 17953 (1994).

[61] G. Kresse and D. Joubert, Phys. Rev. B **59**, 1758 (1999).

[62] N. Metropolis, A. W. Rosenbluth, M. N. Rosenbluth, A. H. Teller, and E. Teller, J. Chem. Phys. **21**, 1087 (1953).

[63] M. Matsumoto and T. Nishimura, ACM Trans. Model. Comput. Simul. **8**, 3 (1998).

[64] T. Saitoh, A. E. Bocquet, T. Mizokawa, H. Namatame, A. Fujimori, M. Abbate, Y. Takeda, and M. Takano, Phys. Rev. B **51**, 13942 (1995).

[65] J. H. Jung, K. H. Kim, D. J. Eom, T. W. Noh, E. J. Choi, J. Yu, Y. S. Kwon, and Y. Chung, Phys. Rev. B **55**, 15489 (1997).

[66] R. Krüger, B. Schulz, S. Naler, R. Rauer, D. Budelmann, J. Bäckström, K. H. Kim, S.-W. Cheong, V. Perebeinos, and M. Rübhausen, Phys. Rev. Lett. **92**, 097203 (2004).

[67] M. W. Kim, S. J. Moon, J. H. Jung, J. Yu, S. Parashar, P. Murugavel, J. H. Lee, and T. W. Noh, Phys. Rev. Lett. **96**, 247205 (2006).

[68] R. Sopracase, G. Gruener, C. Autret-Lambert, V. T. Phuoc, V. Brize, and J. C. Soret, arXiv:cond-mat/0609451.

[69] R. G. Shetkar and A. V. Salker, J. Mater. Sci. Technol. **26**, 1098 (2010).

[70] X. L. Wang, D. Li, T. Y. Cui, P. Kharel, W. Liu, and Z. D. Zhang, J. Appl. Phys. **107**, 09B510 (2010).

[71] P. Negi, G. Dixit, H. M. Agrawal, and R. C. Srivastava, J. Supercond. Novel Magn. **26**, 1611 (2013).

[72] B. C. Hauback, H. Fjellvåg, and N. Sakai, J. Solid State Chem. **124**, 43 (1996).

[73] F. Moussa, M. Hennion, J. Rodriguez-Carvajal, H. Moudden, L. Pinsard, and A. Revcolevschi, Phys. Rev. B **54**, 15149 (1996).

[74] Q. Huang, A. Santoro, J. W. Lynn, R. W. Erwin, J. A. Borchers, J. L. Peng, and R. L. Greene, Phys. Rev. B **55**, 14987 (1997).

[75] D. O'Flynn, C. V. Tomy, M. R. Lees, A. Daoud-Aladine, and G. Balakrishnan, Phys. Rev. B **83**, 174426 (2011).

[76] K. H. Ahn and A. J. Millis, Phys. Rev. B **61**, 13545 (2000).

[77] N. N. Kovaleva, A. V. Boris, C. Bernhard, A. Kulakov, A. Pimenov, A. M. Balbashov, G. Khaliullin, and B. Keimer, Phys. Rev. Lett. **93**, 147204 (2004).

[78] N. N. Kovaleva, A. M. Oleś, A. M. Balbashov, A. Maljuk, D. N. Argyriou, G. Khaliullin, and B. Keimer, Phys. Rev. B **81**, 235130 (2010).

[79] J. He and C. Franchini, Phys. Rev. B **89**, 045104 (2014).

[80] Z. Ergonenc, B. Kim, P. Liu, G. Kresse, and C. Franchini (unpublished).

[81] D. Muñoz, N. M. Harrison, and F. Illas, Phys. Rev. B **69**, 085115 (2004).

[82] R. A. Evarestov, E. A. Kotomin, Y. A. Mastrikov, D. Gryaznov, E. Heifets, and J. Maier, Phys. Rev. B **72**, 214411 (2005).

[83] I. Solovyev, N. Hamada, and K. Terakura, Phys. Rev. Lett. **76**, 4825 (1996).

[84] T. Archer, D. Chaitanya, S. Sanvito, J. He, C. Franchini, A. Filippetti, P. Delugas, D. Puggioni, V. Fiorentini, R. Tiwari *et al.*, Phys. Rev. B **84**, 115114 (2011).

[85] C. Franchini, T. Archer, J. He, X.-Q. Chen, A. Filippetti, and S. Sanvito, Phys. Rev. B **83**, 220402(R) (2011).

[86] N. S. Fedorova, C. Ederer, N. A. Spaldin, and A. Scaramucci, Phys. Rev. B **91**, 165122 (2015).

[87] E. O. Wollan and W. C. Koehler, Phys. Rev. **100**, 545 (1955).